Boundary conditions for the Middle Miocene Climate Transition (MMCT v1.0)

Amanda Frigola[1], Matthias Prange[1,2], Michael Schulz[1,2]

[1]MARUM Center for Marine Environmental Sciences, University of Bremen, Bremen, 28359, Germany

[2]Faculty of Geosciences, University of Bremen, Bremen, 28359, Germany

Correspondence to: Amanda Frigola (afrigola@marum.de)

Abstract. The Middle Miocene Climate Transition was characterized by major Antarctic ice-sheet expansion and global cooling during the interval ~15–13 Ma. Here we present two sets of boundary conditions for global general circulation models characterizing the periods before (Middle Miocene Climatic Optimum; MMCO) and after (Middle Miocene Glaciation; MMG) the transition. These boundary conditions include Middle Miocene global topography, bathymetry and vegetation. Additionally, Antarctic ice volume and geometry, sea-level and atmospheric CO_2 concentration estimates for the MMCO and the MMG are reviewed. The MMCO and MMG boundary conditions have been applied to the Community Climate System Model version 3 (CCSM3) to provide evidence of their suitability for global climate modeling. The boundary-condition files are available for use as input in a wide variety of global climate models and constitute a valuable tool for modeling studies with a focus on the Middle Miocene.

1 Introduction

Our work has its focus on the Middle Miocene Climate Transition (MMCT), an interval of climate change characterized by significant Antarctic ice-sheet expansion and global cooling between ~15 and 13 Ma. Major evidence for this transition is the increase in $\delta^{18}O$ shown in benthic foraminiferal records (e.g. Lear et al., 2010; Shevenell et al., 2008; Holbourn et al., 2005). An increase in benthic foraminiferal $\delta^{18}O$ reflects either an increase in global ice volume or a decrease in bottom water temperature (BWT). Different studies using benthic foraminiferal Mg/Ca ratios (an independent proxy for BWT) to separate the global ice volume from BWT signals in the benthic foraminiferal $\delta^{18}O$ records conclude that both an increase in global ice volume and a decrease in BWT occurred during the MMCT, though global ice volume was the main part (65–85%) in the benthic $\delta^{18}O$ signal (Lear et al., 2010; Lear et al., 2000; Shevenell et al., 2008).

Mg/Ca studies indicate that the cooling of bottom waters across the MMCT would have been within a range of ~0.5 to ~3°C (Lear et al., 2010; Lear et al., 2000; Shevenell et al., 2008; Billups and Schrag, 2002; Billups and Schrag, 2003).

Studies by Kominz et al. (2008) and Haq et al. (1987), based on backstripping techniques, and John et al. (2011), combining backstripping techniques with benthic foraminiferal δ^{18}O, indicate an important eustatic sea-level fall across the MMCT, providing further evidence of ice-sheet expansion. Lewis et al. (2007) present data from glacial deposits in Southern Victoria

30 Land (East Antarctica) showing local ice-sheet expansion at different time intervals between ~13.85 and ~12.44 Ma. They state that this ice-sheet expansion was preceded by significant atmospheric cooling, with glacial deposits showing evidence of a permanent shift from wet to cold in the thermal regime of local glaciers at ~13.94 Ma. Levy et al. (2016) analyze data from the ANDRILL–2A drill site, situated in the western Ross Sea, ~30 km off the coast of Southern Victoria Land. The ANDRILL record presents two unconformities spanning the intervals ~15.8 to ~14.6 Ma and ~14.4 Ma to Late Miocene.

35 These unconformites are interpreted to be caused by local episodes of grounded ice advance eroding material at the site at different times within those two intervals. A global compilation of paleobotanical data by Pound et al. (2012) shows cooling and/or drying in some mid-latitude areas across the MMCT, suggesting that this transition did not only affect high latitudes. The causes for the MMCT are a matter of debate. Suggested driving mechanisms for this transition include a drop in atmospheric pCO_2, changes in ocean circulation and water masses driven by ocean gateways reconfiguration and/or orbitally

40 triggered atmospheric heat and moisture transport variations (Flower and Kennett, 1994; Holbourn et al., 2007; Holbourn et al., 2005).

Our aim is to assemble Middle Miocene boundary conditions for global coupled General Circulation Models (GCMs), setting up an improved basis to investigate the MMCT from a modeling perspective. The boundary conditions include global topography, bathymetry and vegetation for the Middle Miocene. Besides, Antarctic ice volume and geometry, sea-level and

45 atmospheric CO_2 concentration estimates for the periods before (Middle Miocene Climatic Optimum, MMCO) and after (Middle Miocene Glaciation, MMG) the MMCT are reviewed and their uncertainties are discussed. The global topography and bathymetry presented here are mainly based on the Middle Miocene reconstruction by Herold et al. (2008), which has already been used in previous modeling studies (e.g. Herold et al., 2012; Herold et al., 2011; Krapp and Jungclaus, 2011). However, we implement some important modifications with regard to Antarctic ice-sheet geometry, sea-level and

50 configuration of the South East Asian and Panama passages taking into account recent reconstructions. Vegetation cover used in most previous Middle Miocene modeling studies were mainly based on Wolfe's (1985) Early Miocene reconstruction (e.g. Herold et al., 2011; Tong et al., 2009; You et al., 2009). Here, we update these boundary conditions with Middle Miocene data (Pound et al., 2012; Morley, 2011).

Our study provides the core data required to set up GCM experiments with a Middle Miocene configuration. With this

55 configuration as a starting point, a wide variety of sensitivity studies with a focus on the Middle Miocene and its global climate transition can be performed. Despite scarce Middle Miocene data availability and method related uncertainties in the data, our assemblage of boundary conditions reflects the state-of-the-art in Miocene research. Results from two model runs

with the Community Climate System Model version 3 (CCSM3) (Collins et al., 2006) using the MMCO and MMG boundary conditions are also presented.

2 Antarctic ice-sheet geometry

60

Giving quantitative Antarctic ice volume estimates for the MMCT is at best challenging. Most studies present ice volume estimates in units of sea water $\delta^{18}O$. Backstripping methods provide sea-level rather than ice volume estimates. More direct Antarctic ice volume estimates can be derived from modelling studies (Gasson et al., 2016; Langebroek et al., 2009; Oerlemans 2004).

65

Gasson et al. (2016) performed a series of simulations with an ice-sheet model asynchronously coupled to a regional climate model and an isotope-enabled GCM using Middle Miocene palaeogeography and a range of atmospheric CO_2 concentrations and extreme astronomical configurations. The simulations tested two different Antarctic bedrock topography scenarios: one scenario with present day bedrock topography and the other one with an approximate Middle Miocene bedrock topography. For a range of CO_2 concentrations between 500 and 280 ppmv and changing orbital parameters ("warm astronomical configuration" versus "cold astronomical configuration") an increase in Antarctic ice volume from 11.5 (17.2) million km³ in the warmer climate to 26.7 (35.5) million km³ in the colder climate was simulated using modern (Middle Miocene) bedrock topography.

70

Langebroek et al. (2009) used a coupled isotope-enabled ice-sheet–climate model forced by atmospheric CO_2 and insolation changes to reconstruct Antarctic ice volume across the MMCT. The experiment with the best fit to $\delta^{18}O$ data was forced by a CO_2 drop from 640 ppmv to 590 ppmv at around ~13.9 Ma and simulates an increase in Antarctic ice volume from ~6 million to ~24 million km³ across the MMCT.

75

Oerlemans (2004) derived Cenozoic Antarctic ice volume variations by means of a simple quasi-analytical ice-sheet model and two different $\delta^{18}O$ benthic foraminiferal records. The ice-sheet model approximates Antarctic ice volume as a function of deep sea temperature. Using the Zachos et al. (2001) benthic foraminiferal $\delta^{18}O$ data, an ice volume increase from ~5 million to ~23 million km³ for the MMCT was obtained, while for the $\delta^{18}O$ curve by Miller et al. (1987) the increase was only from ~15 million to ~23 million km³.

80

Mainly based on the studies by Oerlemans (2004) and Langebroek et al. (2009), we set a total Antarctic ice-sheet volume of 23 million km³ for the MMG (Table 1; Fig. 1). This value is within the range of published estimates, although smaller than the values estimated by Gasson et al. (2016) in their "cold climate" experiments with extreme astronomical configuration.

85

We opted for using ice-sheet model-derived Antarctic topography estimates from an earlier Cenozoic time period with similar Antarctic ice volume. These data were kindly provided by David Pollard (Pennsylvania State University) and correspond to the Oligocene Oi-1 glaciation event, approximately 34 Ma. They were obtained with a model version close to

that described in Pollard and DeConto (2012), with the main differences being (i) no floating ice shelves, and (ii) climate forcing using a matrix of previous GCM climates for various orbits, CO_2 levels and ice sizes. These topography data provide

90   a fair characterization of the Antarctic ice-sheet at the MMG as they match a total ice volume of 23 million km³. In this topography the whole East Antarctica is covered with a single ice-sheet meanwhile the islands of West Antarctica contain only some small ice caps, with no marine-based ice-sheets (Fig. 1).

For the MMCO we assume a total Antarctic ice-sheet volume of 6 million km³ (Table 1, Fig. 1). This 6 estimate is in good agreement with the values given by Langebroek et al. (2009) and Oerlemans (2004), although significantly lower than

95   Gasson et al. (2016) (see above).

To characterize the MMCO Antarctic topography, again David Pollard's data from the same Oi-1 simulation were used, which match an Antarctic ice volume of 6 million km³. In this topography Antarctica is only partially glaciated, with an ice cap covering the Transantarctic Mountains and another one over eastern East Antarctica. Again, West Antarctica contains only some ice caps, with no marine based ice-sheets (Fig. 1).

100   The ice volume values of 6 million and 23 million km³ for the MMCO and the MMG, respectively, imply an increase of 17 million km³ across the MMCT. This value is within the range of published estimates and in reasonable agreement with the values by Langebroek et al. (2009), Oerlemans (2004) as well as Gasson et al. (2016) (see above).

Although some studies suggest ice would have been present in the Northern Hemisphere during the Middle Miocene (Thiede et al., 2011; DeConto et al., 2008), very few is known about its temporal and spatial distribution. In view of the lack of

105   concrete data, Northern Hemisphere ice was neglected in the current study.

3 Sea-level change across the MMCT

Lear et al. (2010) combine Mg/Ca and Li/Ca ratios to estimate BWT at ODP Site 761 across the MMCT. Sea water $\delta^{18}O$ is then derived by extracting the BWT signal from the $\delta^{18}O$ signal from the same site. The data suggest an increase in sea water $\delta^{18}O$ of 0.6 per mil between 15.3 and 12.5 Ma. This value is converted into a sea-level fall equivalent using the Pleistocene

110   calibration of 0.08–0.11 per mil per 10 m sea-level (Fairbanks and Matthews, 1978), obtaining an eustatic sea-level drop of ~55–75 m between 15.3 and 12.5 Ma.

Langebroek et al. (2009) suggested Antarctic ice volumes of ~6 million and ~24 million km³ for the MMCO and the MMG, respectively (see previous Sect.). These ice volume estimates can be converted into sea-level equivalents according to:

$$S_{eq} = (\rho_{ice}*V_{ice}) / (\rho_{water}*A_0) \qquad (1)$$

115   where S_{eq} represents sea-level equivalent, V_{ice} ice-sheet volume, ρ_{ice} density of ice, ρ_{water} density of water and A_0 ocean surface area. With $\rho_{ice} = 910$ kg/m³, $\rho_{water} = 1000$ kg/m³ and $A_0 = 360.5$ million km² (present-day approx.), the resulting sea-

level equivalents are ~16 and ~59 m for the MMCO and MMG, respectively, implying a sea-level fall of ~43 m across the MMCT.

De Boer et al. (2010) used one-dimensional ice-sheet models and benthic foraminiferal $\delta^{18}O$ data (Zachos et al., 2008) to
120 derive eustatic sea-level and BWT changes over the last 35 Ma. In their approach, surface air temperature has been derived through an inverse procedure from the benthic $\delta^{18}O$ record. The study suggests a sea-level drop of ~40 m between 15 and 12 Ma, i.e., from ~55 to ~15 m above present-day.

Kominz et al. (2008) combine data from different boreholes collected from the New Jersey and Delaware Coastal Plains to derive sea-level for the last 108 Ma through backstripping. They register a ~20 m sea-level fall between ~14.2 and ~12.8 Ma,
125 i.e., from ~25 to ~5 m above present day. These data contain some unconformities however, implying that the actual amplitude of the MMCT sea-level drop could have been indeed higher than proposed there.

John et al. (2011) estimate Middle Miocene sea-level changes based on backstripping and benthic foraminiferal oxygen isotope data. Backstripping is applied to sediment core data from the Marion Plateau, offshore Northeastern Australia, obtaining a range of sea-level variations which is then further constrained using benthic foraminiferal $\delta^{18}O$ data from Zachos
130 et al. (2001). John et al. (2011) suggest a 53–69 m sea-level fall between 16.5 and 13.9 Ma. Unfortunately, their analyses are limited to this time interval.

For the sake of coherency within the current set of Middle Miocene boundary conditions, we opted for a sea-level change across the MMCT that is consistent with our ice-sheet volume estimates for the MMCO and MMG (see previous Sect.), presuming that global sea-level change across the MMCT time interval was dominated by glacio-eustasy. The ice-sheet
135 volume estimates were converted into sea-level equivalents according to Eq. (1), obtaining values of 16 and 59 m for the MMCO and the MMG respectively, and thus a sea-level fall across the MMCT of 43 m (Table 1).

A sea-level fall of 43 m across the MMCT is consistent with Langebroek et al. (2010) (~43 m) and in good agreement with the study by De Boer et al. (2010) (~40 m), although somewhat larger than the values by Gasson et al. (2016) (~30–36 m) and considerably higher than Kominz et al. (2008) estimate (~20 m of sea-level fall). By contrast, John et al. (2011) suggest
140 a higher amplitude of sea-level drop (~53–69 m), similar to the ~55–75 m by Lear et al. (2010). As such, our assumption of 43 m sea-level fall lies well within the range of published estimates.

4 Atmospheric CO$_2$ concentration

Middle Miocene atmospheric pCO$_2$ is a matter of debate as different studies suggest significantly different pCO$_2$ levels. Based on planktonic foraminiferal boron isotopic data, Foster et al. (2012) suggest atmospheric pCO$_2$ values reaching a
145 maximum of ~390 ppmv at ~15.8 Ma and decreasing to ~200 ppmv by ~12 Ma. Pearson and Palmer (2000), using the same method, obtain a maximum value of ~300 ppmv at ~16.2 Ma followed by a decline to ~140 ppmv by ~14.7 Ma and an

increase to ~225 ppmv by ~11.4 Ma. Tripati et al. (2009), by means of surface-dwelling foraminiferal boron/calcium ratios, obtain a maximum value of ~430 ppmv at ~15.1 Ma followed by a decrease to ~340 ppmv by ~12 Ma and down to ~230 ppmv by ~9.9 Ma. Retallack (2009), based on carbon isotopes of pedogenic carbonate, suggests atmospheric pCO_2 levels

150 reaching a maximum of ~850 ppmv at ~15.6 Ma, dropping down to ~115 ppmv by ~14.6 Ma and increasing to ~430 ppmv by ~12.8 Ma. Kuerschner et al. (2008) used stomatal-density data from fossil leaves to support pCO_2 values reaching a maximum over ~400–500 ppmv at ~15.5 Ma, decreasing to ~280 ppmv by ~14 Ma and increasing to ~340 ppmv by ~12 Ma. By contrast, Pagani et al. (2005), using a method based on alkenone carbon isotopes, obtain pCO_2 values oscillating between ~200 ppmv and ~300 ppmv across the Middle Miocene.

155 In spite of the tremendous discrepancies between studies, all except for Pagani et al. (2005) agree on an atmospheric pCO_2 drawdown starting at the MMCO. The exact magnitude of this decrease is however not clear: ~190 ppmv between ~15.8 and ~12 Ma according to Foster et al. (2012), ~160 ppmv between ~16.2 and ~14.7 Ma or ~75 ppmv between ~16.2 and ~11.5 Ma according to Pearson and Palmer (2000), ~90 ppmv between ~15.1 and ~12 Ma or ~200 ppmv between ~15.1 and ~9.9 Ma according to Tripati et al. (2009), ~740 ppmv between ~15.6 and ~14.6 Ma or ~420 ppmv between ~15.6 and ~12.8 Ma

160 according to Retallack (2009), and over ~120–220 ppmv between ~15.5 and ~14 Ma or over ~60–160 ppmv between ~15.5 and ~12 Ma according to Kuerschner et al. (2008).

We chose atmospheric CO_2 concentrations of 400 ppmv and 200 ppmv to represent the MMCO and the MMG respectively (Table 1). Although somewhat arbitrary, these values are within the range of published estimates. The 400 ppmv MMCO estimate represents a maximum rather than a mean (within the interval ~15–17 Ma) and is in favourable agreement with

165 Foster et al. (2012) and Tripati et al. (2009), as well as with the most recent alkenone- and boron isotope-based pCO_2 reconstructions for the MMCO by Zhang et al. (2013) and Greenop et al. (2014). The 200 ppmv MMG estimate represents a minimum rather than a mean (within the interval ~12–15 Ma) and is in good agreement with Foster et al. (2012) and Pagani et al. (2005).

5 Global topography and bathymetry

170 We present here two different global Middle Miocene topography/bathymetries, characterizing the MMCO and the MMG periods (Fig. 2, Table 1). Both global topography/bathymetries are mainly based on the 2°x2° reconstruction of Herold et al. (2008), although some important modifications, which will be described below, were applied to their original dataset. To reconstruct paleogeography and paleotopography Herold et al. (2008) used a global plate rotation model and geological data. Ocean depth was reconstructed by applying an age–depth relationship to a global Middle Miocene isochron map. Sediment

175 thickness and large igneous provinces were also considered in the reconstruction of ocean depth.

In Herold et al. (2008), the Andes and the Tibetan plateau were set with estimated Early to Middle Miocene elevations. The Rocky mountains and the east African topography were reduced to 75 and 25% of their current elevation, respectively. The Greenland topography was also reduced, representing ice free conditions. The Bering Strait was closed and the Hudson Bay removed. Unlike Herold et al. (2008), who assumed the Tethys seaway closed, we decided to leave the seaway open.

180 According to Rögl (1999), the Tethys passage closed during the Burdigalian (20.44–15.97 Ma), re-opened temporary during the Langhian (15.97–13.65 Ma) and closed again during the Serravallian (13.65–11.62 Ma). Also based on Rögl (1999), the Parathethys was intermittently connected and disconnected from the global ocean during the Burdigalian to Serravallian interval. In Herold et al. (2008), as in our reconstruction, the Parathethys is connected to the global ocean. In view of the variable configuration of the Tethys/Parathethys across the Middle Miocene, it would be recommendable to test different

185 Tethys/Parathethys configurations when performing Middle Miocene experiments with GCMs, although such testing can be limited by model constraints: seas disconnected from the global ocean can produce freshwater imbalance in GCMs and narrow ocean passages require high resolution ocean grids to allow ocean flux calculation (Rosenbloom et al., 2011). Some studies, indeed, suggest that the Tethys passage closure might have played a role in Middle Miocene atmosphere and ocean circulation patterns (Ramstein et al., 1997; Hamon et al., 2013).

190 Some important modifications were applied to the original dataset of Herold et al. (2008) regarding Antarctic ice-sheet geometry, sea-level and configuration of the South East Asian and Panama passages.

5.1 Antarctica

Antarctic ice-sheet geometry was modified for consistency with our ice-sheet volume estimates for the MMCO and MMG (see Sect. 2). In the high southern latitudes, from 60°S to 90°S, the original topography/bathymetry from Herold et al. (2008)

195 was replaced by the Antarctic topography/bathymetry data from David Pollard described above (Fig. 1e,f).

5.2 Sea-level

Sea-level was adjusted to ~48 m and ~5 m above present-day for the MMCO and MMG, respectively (Table 1). These values were derived from our sea-level equivalent estimates (see above) by assuming 64 m of present-day sea-level equivalent. The adjustments were applied taking into account that sea-level is ~52 m above present-day in Herold et al.

200 (2008) (Nicholas Herold, pers. comm.) and at present-day level in David Pollard's data. We note that the sea-level adjustment of 4 m (i.e. 48 m above present-day instead of 52 m) of Herold et al. (2008) for the MMCO is minor and has virtually no effect in common global climate models at low spatial resolution.

5.3 South East Asian gateway

South East Asian paleogeography was modified based on Hall's (2012) reconstruction constrained at 15 Ma (Fig. 3). This
205 reconstruction was available in jpg format as a georeferenced image. The data needed thus to be converted into grid format
before they could be embedded into the global topography/bathymetry datasets. We used ArcGIS:
https://www.arcgis.com/home/index.html for that purpose. Qualitative height/depth values were assigned to the different
geographic features described in Hall (2012): ~2800 m for volcanoes, ~1000 m for highlands, ~250 m for land, ~-22 m for
carbonate platforms, ~-200 m for shallow sea, <-4000 m for deep sea, and ~-5500 m for trenches. The border regions
210 between the different geographic features were assigned intermediate values, in order to avoid too steep bathymetry
gradients that could cause model computational problems. After that, the data were embedded into the MMCO global
topography/bathymetry dataset. Further minor manual smoothing was applied at the margins of the embedded region. Here,
shallow bays were removed and single, shallow grid points surrounded by much deeper grid points were deepened to the
adjacent depth. In total, these modifications affected ~0.5% of the total number of grid points.

215 Based on the depth values assigned to the different geographic features in the South East Asia reconstruction, the deepest
connection between the Indian and the Pacific Ocean would be only ~200 m deep. This is probably too shallow, since in the
Middle Miocene the Indonesian gateway was likely open for both surface and intermediate water (Kuhnt et al., 2004). Deep
water passages were therefore added to the MMCO global topography/bathymetry dataset, based on the postulated Middle
Miocene ocean paths across the Indonesian archipelago described in Kuhnt et al. (2004) (Fig. 3). The depth values assigned
220 to these passages are shallower than those of the present-day passages (Kuhnt et al., 2004). Based on an educated guess the
depths of the two eastern passages were set to 800 m, shallower than that of the present-day eastern Lifamatola (~1940 m)
and Timor (~1300–1450 m) passages (Gordon et al., 2003). The northwestern passage was assigned a depth of 1000 m,
shallower than that of the present-day northwestern Sangihe Ridge sill (~1350 m) (Gordon et al., 2003). The depth of the
southwestern passage was set to 600 m, slightly shallower than that of the present-day southwestern Dewakang sill (680 m)
225 (Gordon et al., 2003). Assigned widths are somewhat arbitrary. The eastern passages were both given a width of ~150 km
(~3 grid cells), and the northwestern and southwestern passages a width of ~350 km (~6 grid cells) and ~220 km (~4 grid
cells) respectively.

For the MMG, the same South East Asia topography/bathymetry reconstruction was used as for the MMCO after applying a
~43 m sea-level change, in correspondence with our MMCT sea-level fall estimate (see above).

5.4 Panama passage
230

Also the Panama passage was modified such that substantial differences exist compared to Herold et al. (2008) original
dataset. Montes et al. (2012) suggest a narrow Panama strait already by the Early Miocene, with a width of ~200 km.

Therefore, the width of the seaway was set accordingly in our paleogeographic dataset, together with a depth of ~1000 m which reflects Panama sill reconstructions for the Middle Miocene by Duque-Caro (1990).

235 **6 Global vegetation**

The current MMCO and MMG global vegetation reconstructions (Fig. 4) were based on Pound et al. (2012), Wolfe (1985) and Morley (2011). The study by Pound et al. (2012) includes global vegetation reconstructions for the Langhian (15.67–13.65 Ma) (approximately the end of the MMCO) and the Serravallian (13.65–11.61 Ma) (roughly coincident with the MMG). Wolfe's (1985) study contains an Early Miocene global vegetation reconstruction. The reconstructions from Pound
240 et al. (2012) and Wolfe (1985) are the only Early/Middle Miocene global reconstructions. Morley's (2011) Middle Miocene reconstruction focuses only on the distribution of tropical forests.

The study by Pound et al. (2012), based on paleobotanical evidence from 617 Middle/Late Miocene data locations, constituted the main source of global vegetation data for our MMCO and MMG boundary conditions. Morley's (2011) study added some detail to the current reconstructions in the tropical areas. Wolfe's (1985) Early Miocene data were used in
245 regions where the Middle Miocene reconstructions by Pound et al. (2012) and Morley (2011) had scarce data coverage and also to characterize the vegetation patterns of the main mountain ranges.

The above studies use different nomenclatures to classify the different types of vegetation. Pound et al. (2012) use the BIOME4 classification (Kaplan, 2001), while Wolfe (1985) uses the classification scheme described in Wolfe (1979). Here, we coded the data in the Land Surface Model (LSM) (Bonan, 1996) biome classification scheme. Table 2 shows how the
250 data from Pound et al. (2012), Wolfe (1985) and Morley (2011) were converted into the LSM scheme. However, we note that the correspondence between biomes of different schemes is not always optimal (see notes in Table 2). Note also that Table 2 does not contain all the biomes present in the different vegetation schemes, but only the ones effectively used in the current reconstructions. All biome names in the following are italized, with LSM biome names in addition set in quotation marks.

255 Neither Pound et al. (2012) nor Wolfe (1985) or Morley (2011) provide the data in a gridded format, a requirement for the use in GCMs. According to the geographical coordinates specified in those reconstructions, we merged the data on a 2°x2° latitude/longitude grid for MMCO and MMG, giving preference to the Middle Miocene reconstructions by Pound et al. (2012) and Morley (2011). The Early Miocene reconstruction of Wolfe (1985) was only used at locations where no data are available from the other two reconstructions. An exception are the Alps, Rocky Mountains, Himalayas and Tibetan Plateau,
260 where we used the information from Wolfe (1985). At the regions where the reconstructions from Pound et al. (2012) and Morley (2011) were conflicting with each other, the reconstruction of Pound et al. (2012) was used, except for locations where the latter was less well constrained by proxy information than Morley (2011).

The MMCO and the MMG global vegetation reconstructions presented here solely differ in terms of *"tundra"* distribution on Antarctica (Fig. 4). In both reconstructions *"tundra"* was assigned to the ice free regions of Antarctica, taking account of the

265   MMCO and MMG ice-sheet geometries (Fig. 1c,d). Assuming the *"tundra"* distribution to be the only difference in terms of vegetation between the MMCO and the MMG is a simplification. Part of the *warm-temperate evergreen broadleaf and mixed forest* (*"warm mixed forest"* in the LSM scheme) present in the middle latitudes during the Langhian was replaced by "cooler and/or drier temperate biomes" during the Serravallian (Pound et al., 2012). This cooling and/or drying trend was observed for example in areas like western North America or Europe (Pound et al., 2012). Additionally, by the Serravallian,

270   in the tropics, some drier biomes than those present there during the Langhian had started to spread (e.g. in South East Asia) (Pound et al., 2012). Nevertheless, the Langhian and Serravallian global vegetation patterns were similar (Pound et al., 2012), which justifies our simplified approach.

We are aware that the Middle Miocene global vegetation reconstructions presented here are rather coarse. Still, we consider it a fair characterization of the MMCO and MMG global vegetation distributions. Grosso modo, the present reconstructions

275   are characterized by *"cool mixed forest"* at high northern latitudes, predominantly *"warm mixed forest"* at middle latitudes, *"tropical broadleaf evergreen forest"* in the tropics, and *"tundra"* in the ice free regions of Antarctica (Fig. 4).

6.1 Europe

The most widespread biome in the middle latitudes of Europe during the Langhian was the *warm-temperate evergreen broadleaf and mixed forest* (*"warm mixed forest"*) (Pound et al., 2012). On the southern and eastern coast of Spain however,

280   drier biomes such as *temperate xerophytic shrubland* (*"evergreen shrub land"/"deciduous shrub land"*) or *temperate deciduous broadleaf savanna* (*"deciduous shrub land"*) were present (Pound et al., 2012) (Fig. 4). The vegetation patterns of the Serravallian were similar to those of the Langhian. However, some drying and/or cooling occurred. In east Europe, for example, the data by Pound et al. (2012) indicate the emergence of *temperate deciduous broadleaf savanna* (*"deciduous shrub land"*). These drier and/or cooler biomes developed during the Serravallian were neglected for simplification in the

285   current reconstructions.

Evidence for the Middle Miocene European high northern latitudes (above 60°N) is missing in Pound et al. (2012). This region was painted with *mixed coniferous forest* (*"cool mixed forest"*) (Fig. 4) in the current MMCO and MMG reconstructions based on Wolfe's (1985) Early Miocene data. We also filled the Alpine area with *mixed coniferous forest* (*"cool mixed forest"*) according to Wolfe (1985).

290   6.2 Asia

The Asian high northern latitudes were assigned *"cool mixed forest"* in the current MMCO and MMG reconstructions (Fig. 4). Pound et al. (2012) suggest *cool-temperate mixed forest* (*"cool mixed forest"*) to have been the dominant biome in the

eastern Asian high northern latitudes during the Middle Miocene. No data are provided for the western Asian high northern latitudes in Pound et al. (2012). Wolfe's (1985) reconstruction suggests two different vegetation patterns for the western

295 Asian high northern latitudes during the Early Miocene, corresponding to north and south. For simplification, only the northern pattern, consisting of *mixed coniferous forest* (*"cool mixed forest"*), was considered in the current reconstructions.

The western Asian middle latitudes were filled with *"warm mixed forest"* (Fig. 4). Pound et al. (2012) propose a "south to north drying and cooling trend" for that region during the Middle Miocene, starting with *warm-temperate evergreen broadleaf and mixed forest* (*"warm mixed forest"*) in the southern part and ending with *temperate deciduous broadleaf*

300 *savanna* (*"deciduous shrub land"*) in the northern part. For simplification, only the *warm-temperate evergreen broadleaf and mixed forest* (*"warm mixed forest"*) was considered in our current MMCO and MMG boundary conditions.

The Himalayas and the Tibetan Plateau were assigned *mixed coniferous forest* (*"cool mixed forest"*) based on Wolfe's (1985) reconstruction.

The eastern Asian middle latitudes were mainly populated by *warm-temperate evergreen broadleaf and mixed forest* (*"warm

305 mixed forest"*) during the Middle Miocene (Pound et al., 2012) (Fig. 4). Along the coast at ~32°N, there was a *tropical evergreen broadleaf forest* (*"tropical broadleaf evergreen forest"*), and west of 111°E a drier region containing biomes such as *temperate xerophytic shrubland* (*"evergreen shrub land"/"deciduous shrub land"*) (Pound et al., 2012). This drier region was dismissed for simplification in our MMCO and MMG reconstructions.

Tropical evergreen broadleaf forest (*"tropical broadleaf evergreen forest"*) was the dominant biome in India and South East

310 Asia during the Middle Miocene (Pound et al., 2012) (Fig. 4).

6.3 Australia and New Zealand

Tropical evergreen broadleaf forest (*"tropical broadleaf evergreen forest"*) was present in northeast Australia during the Middle Miocene (Pound et al., 2012) (Fig. 4). Also in the east, but south of 28°S, *warm-temperate evergreen broadleaf and mixed forest* (*"warm mixed forest"*) was present (Pound et al., 2012).

315 In Pound et al. (2012) the description of Australia is limited to the east side. A line of *megathermal rain forest* (*"tropical broadleaf evergreen forest"*) was assigned along the north coast in the current reconstructions based on Morley's (2011) Middle Miocene data.

Wolfe's (1985) Early Miocene reconstruction suggests the vegetation patterns of east Australia to be also representative for central Australia. Assuming this would still be valid during the Middle Miocene, the *"warm mixed forest"* assigned to east

320 Australia in the current reconstructions, was extended to central Australia.

Wolfe's (1985) data further suggest similar vegetation patterns for west Australia and the southern coast of Spain during the Early Miocene. Assuming this analogy to be still valid during the Middle Miocene, west Australia was filled with

"*evergreen shrub land"/"deciduous shrub land"*, which is the vegetation assigned to the southern coast of Spain in the current MMCO and MMG reconstructions.

325 *Warm-temperate evergreen broadleaf and mixed forest* (*"warm mixed forest"*) occupied New Zealand during the Middle Miocene (Pound et al., 2012) (Fig. 4).

6.4 Antarctica

There is evidence for *low- and high-shrub tundra* and *prostrate dwarf-shrub tundra* (*"tundra"*) at the Antarctic margins during the Langhian (Pound et al., 2012). By the Serravallian, practically no vegetation was present on Antarctica (Pound et

330 al., 2012). In the current MMCO and MMG reconstructions *"tundra"* was assigned to the ice free regions, in consistence with the ice-sheet geometries described above (Fig. 4).

6.5 Africa and the Arabian Peninsula

Africa and the Arabian Peninsula have poor data coverage in Pound et al. (2012). Evidence from Pound et al. (2012) for the most northern part of Africa for the Middle Miocene is restricted to one site (in Tunisia), suggesting a *warm-temperate*

335 *evergreen broadleaf and mixed forest* (*"warm mixed forest"*). That data site was dismissed in our current MMCO and MMG reconstructions, in view of the inappropriateness to extrapolate data from only one site to the whole surrounding region. Instead, the most northern part of Africa was set to *"evergreen shrub land"/"deciduous shrub land"* (Fig. 4). Wolfe's (1985) Early Miocene reconstruction suggests similar vegetation patterns for that region as for the southern coast of Spain. Assuming these two regions kept similar vegetation patterns also during the Middle Miocene, *"evergreen shrub*

340 *land"/"deciduous shrub land"*, the vegetation assigned to the southern coast of Spain in the current MMCO and Middle MMG reconstructions, was also assigned to the most northern part of Africa. Also a narrow belt of *megathermal rain forest* (*"tropical broadleaf evergreen forest"*) was set along the northwest coast, in agreement with Morley's (2011) Middle Miocene reconstruction.

Madagascar was assigned *megathermal rain forest* (*"tropical broadleaf evergreen forest"*), following Morley (2011). Also

345 based on Morley's (2011) reconstruction, an area of *megathermal rain forest* (*"tropical broadleaf evergreen forest"*) was defined along the south and southeast coast of southern Africa. Pound et al. (2012) suggest that drier tropical biomes, e.g. *tropical savanna* (*"savanna"*), were present close to the southern coast of southern Africa during the Middle Miocene. These drier biomes were dismissed for simplification in our MMCO and MMG boundary conditions.

Still in southern Africa, north of the *"tropical broadleaf evergreen forest"* line, a region of *"warm mixed forest"* was

350 assigned. Wolfe (1985) suggests similar vegetation patterns for that region and for southeast Australia during the Early Miocene. Assuming those two regions kept similar vegetation patterns also during the Middle Miocene, *"warm mixed*

forest", the biome set for southeast Australia in the current MMCO and MMG reconstructions, was also assigned to that region.

The remaining areas of Africa and the Arabian Peninsula were assigned *"tropical broadleaf evergreen forest"*, although we
355   are aware that this is probably too broad for a characterization, as also drier tropical biomes were present. Wolfe (1985) suggests that *tropical rain forest* (*"tropical broadleaf evergreen forest"*) and other drier tropical biomes populated that region during the Early Miocene. Pound et al. (2012) show occurrence of *tropical evergreen broadleaf forest* (*"tropical broadleaf evergreen forest"*) in equatorial Africa during the Middle Miocene, although combined with drier tropical biomes like *tropical deciduous broadleaf forest and woodland* (*"tropical broadleaf deciduous forest"*) or *tropical savanna*
360   (*"savanna"*). On the Arabian Peninsula, a single site indicates *tropical deciduous broadleaf forest and woodland* (*"tropical broadleaf deciduous forest"*) existed in that area during the Langhian (Pound et al., 2012). These drier tropical biomes were dismissed for simplification in our boundary conditions.

6.6 North America and Greenland

During the Middle Miocene, the western North American high latitudes were populated with *cool-temperate mixed forest*
365   (*"cool mixed forest"*) (Pound et al., 2012) (Fig. 4). Evidence for the eastern North American high latitudes is missing in Pound et al. (2012). Wolfe (1985) suggests two different patterns for the eastern North American high latitudes during the Early Miocene, at ~60°–65°N and north of ~65°N, respectively. For simplification only the most northern pattern, *mixed coniferous forest* (*"cool mixed forest"*), was considered in the current MMCO and MMG reconstructions.

During the Langhian, *warm-temperate evergreen broadleaf and mixed forest* (*"warm mixed forest"*) was prevalent in the
370   western North American middle latitudes above 40°N (Pound et al., 2012). South of 40°N a drier region existed, with biomes such as *temperate xerophytic shrubland* (*"evergreen shrub land"*/*"deciduous shrub land"*) (Pound et al., 2012) (Fig. 4). During the Serravallian, the western North American middle latitudes became more heterogeneous in terms of vegetation, an amalgam of *warm-temperate evergreen broadleaf and mixed forest* (*"warm mixed forest"*) combined with other drier and/or cooler biomes (Pound et al., 2012). For simplification, the Langhian pattern was used in both MMCO and MMG
375   reconstructions.

The Rocky Mountains were set to *mixed coniferous forest* (*"cool mixed forest"*) following Wolfe (1985).

The central North American middle latitudes were assigned *"warm mixed forest"* in the current MMCO and MMG reconstructions based on Wolfe (1985). That region has scarce data coverage in Pound et al. (2012) (one Langhian site, two Serravallian sites). Wolfe (1985) suggests two different patterns for the central North American middle latitudes during the
380   Early Miocene, corresponding to south and north. For the southern part, Wolfe (1985) suggests similar vegetation patterns as for southeast Australia (assigned *"warm mixed forest"* here), and for the northern part, similar vegetation patterns as for the European middle latitudes (assigned *"warm mixed forest"* here).

However, the central North American middle latitudes were not exclusively vegetated by *"warm mixed forest"* during the Middle Miocene. Wolfe (1985) suggests the presence of "at least some interfluve grassland" in areas such as Nebraska during the late Middle Miocene. Besides, Pound et al. (2012) show some evidence for the presence of *temperate grassland* (*"cool grassland"*) (Langhian) and *temperate deciduous broadleaf savanna* (*"deciduous shrub land"*) (Serravallian) in the central American middle latitudes during the Middle Miocene. These biomes were, however, dismissed for simplification in our current reconstructions.

The eastern North American middle latitudes were also assigned *"warm mixed forest"* in the current MMCO and MMG reconstructions. Pound et al. (2012) suggest *warm-temperate evergreen broadleaf and mixed forest* (*"warm mixed forest"*) existed in eastern North America between 29°N and 39°N, both during the Langhian and the Serravallian. However, outside that interval of latitude no data were available from Pound et al. (2012). Since Wolfe (1985) suggests similar vegetation patterns for the central and eastern North American middle latitudes during the Early Miocene, assuming this analogy would still be valid during the Middle Miocene, *"warm mixed forest"* was also applied to the east, north of 39°N and south of 29°N.

No Middle Miocene data were available for Greenland from Pound et al. (2012). North Greenland was filled with *mixed coniferous forest* (*"cool mixed forest"*) in our current reconstructions based on Wolfe (1985). South Greenland was assigned *"warm mixed forest"*, given its similar latitudinal position and relative geographic proximity with Iceland, where *warm-temperate evergreen broadleaf and mixed forest* (*"warm mixed forest"*) existed during the Middle Miocene according to Pound et al. (2012).

6.7 Central America and south Mexico

Central America and southern Mexico were assigned *"tropical broadleaf evergreen forest"* (Fig. 4). Morley (2011) suggests *megathermal rain forest* (*"tropical broadleaf evergreen forest"*) populated that region in the Middle Miocene. Pound et al. (2012) suggest that the *tropical evergreen broadleaf forest* (*"tropical broadleaf evergreen forest"*) coexisted with drier tropical biomes (Langhian) and with temperate biomes (Langhian and Serravallian), and proposes altitude as an explanation for the presence of temperate biomes in that region during the Middle Miocene. The drier tropical biomes and the temperate biomes were dismissed in our current MMCO and MMG reconstructions for simplification.

6.8 Northern South America

In northern South America, the northern half and the east were filled with *"tropical broadleaf evergreen forest"* in our reconstructions (Fig. 4). Pound et al. (2012) suggest *tropical evergreen broadleaf forest* (*"tropical broadleaf evergreen forest"*) as the main biome in that region during the Langhian and Serravallian. Nevertheless, they also show evidence for some *tropical deciduous broadleaf forest and woodland* (*"tropical broadleaf deciduous forest"*) in that region during the

Serravallian. Morley (2011) suggests the presence of *megathermal rain forest ("tropical broadleaf evergreen forest")* and *monsoonal megathermal forest (*"tropical broadleaf deciduous forest")* in that region during the Middle Miocene. The

415 "*tropical broadleaf deciduous forest*" was neglected for simplification in our boundary conditions.

No data were available from Pound et al. (2012) or Morley (2011) for the southwestern part of northern South America. Within that area, the Andes were assigned *"warm mixed forest"* and the rest *"tropical broadleaf evergreen forest"*. For the Early Miocene Andes, Wolfe (1985) suggests similar vegetation patterns as for the most southern part of southern South America. Since significant uplift of the Andes would have started only in the late Miocene (Ghosh et al., 2006), we

420 considered reasonable to assume that these regions kept similar vegetation patterns also during the Middle Miocene. In this way, *"warm mixed forest"*, the biome set in our data for the most southern part of South America (see below), was also assigned to the Andes. Surrounding the Andes there is another area with non-tropical biomes in Wolfe's (1985) reconstruction, which was dismissed here for simplification. The rest of southwest northern South America is occupied by *tropical rain forest* and *paratropical rain forest* (*"tropical broadleaf evergreen forest"*) in Wolfe's (1985) reconstruction.

425 **6.9 Southern South America**

During the Middle Miocene, in the northwest of southern South America, there was a region covered by arid biomes such as *temperate xerophytic shrubland* (*"evergreen shrub land"/"deciduous shrub land"*) (Pound et al., 2012) (Fig. 4).

In the northeast, along the coast, a narrow belt of *megathermal rain forest* (*"tropical broadleaf evergreen forest"*) was present according to Morley's (2011) Middle Miocene reconstruction.

430 No evidence from Pound et al. (2012) or Morley (2011) was available for the area between the arid region in the west and the *"tropical broadleaf evergreen forest"* in the east. East of the arid region, for the area corresponding to the Andes, Wolfe (1985) proposes similar vegetation patterns for the Early Miocene as for the most southern part of southern South America. Assuming these two areas kept similar vegetation patterns also during the Middle Miocene, *"warm mixed forest"*, the biome set in the current MMCO and MMG reconstructions for the most southern part of southern South America (see below), was

435 also assigned to that part of the Andes. For the region east of the Andes, for the Early Miocene, Wolfe (1985) proposes a vegetation pattern similar to that of southeast Australia. Assuming this analogy kept being valid also during the Middle Miocene, *"warm mixed forest"*, the biome set in the current Middle Miocene reconstructions for southeast Australia, was assigned to that region.

The south of southern South America was filled with *"warm mixed forest"* in our MMCO and MMG reconstructions (Fig. 4).

440 Pound et al. (2012) shows evidence for *warm-temperate evergreen broadleaf and mixed forest* (*"warm mixed forest"*) mixed with *temperate grassland* (*"cool grassland"*) south of 35°S, and again for *warm-temperate evergreen broadleaf and mixed forest* (*"warm mixed forest"*) at 55°S. The *temperate grassland* (*"cool grassland"*) south of 35°S was dismissed here for simplification.

7 Testing the boundary conditions with CCSM3

445 To provide evidence of the suitability of our input data for global climate modeling, we applied the boundary conditions to the Community Climate System Model version 3 (CCSM3). CCSM3 is a fully coupled GCM consisting of components representing atmosphere, ocean, land and sea ice (Collins et al., 2006). A total of three runs were performed: two Miocene runs (MMCO and MMG) and a pre-industrial control run (PI). For the PI run, the standard configuration T42x1 was used. In that configuration, the atmosphere horizontal grid resolution corresponds to a spectral truncation of T42 (~2.8°). The land

450 and atmosphere models share the same horizontal grid. The horizontal ocean grid is a dipole grid with 384 points in latitude and 320 points in longitude. The zonal resolution is ~1°, the mean meridional resolution is ~0.5°, refined around the equator (~0.3°). The ocean and sea–ice components share the same horizontal grid. The atmosphere and ocean vertical grids have 26 and 40 vertical levels, respectively. For the Miocene runs the same grids as for the PI run were used, except for the horizontal ocean (and sea–ice) grid, for which a customized grid was used. This grid is also a dipole grid with 384 points in

455 latitude and 320 points in longitude, although extended to ~87°S (instead of ~79°S) in order to accommodate the changes in the bathymetry off West Antarctica. In the Miocene topography/bathymetry datasets West Antarctica is for the most below sea-level, with ocean reaching down to ~85°S. If the standard CCSM3 grid had been used for the Miocene experiments, the ocean region between ~79°S and 85°S would not have been taken into account in the ocean circulation simulations.

For the PI run, greenhouse gases, aerosols, solar constant and orbital configuration were set according to Otto-Bliesner et al.

460 (2006). The boundary conditions summarized in Table 1 were used for the Miocene experiments. Greenhouse gases, aerosols and solar constant were kept the same as in PI, except for CO_2 (Table 3). The orbital configuration differed from the PI setup. Obliquity was set to 23.24° (mean value for the interval 13-15 Ma), eccentricity to 2.13×10^{-4} (minimum during the last 51 Ma in order to minimize the effect of precession), and precession kept at 102.92° (present-day) (Laskar et al., 2004). The PI experiment was branched from the NCAR CCSM3 1870 CE control run (archived as b30.043) and integrated another 150

465 years (850 years in total). The Miocene experiments were integrated for a total of 1500 years. The last 100 years of each simulation were used for the analysis.

Figure 5 shows mean annual precipitation and sea-surface temperature (SST) for the MMCO and MMG simulations relative to the control run. Some patterns distinguishing the Miocene runs from the PI run include lower precipitation rates during the Miocene along the northwest coast of South America (15°S-10°N)(up to 5-6 mm/day lower), although reaching further

470 inland. In central Africa, between 20°S-5°N, the results show values up to 3-4 mm/day lower than PI. In the Indian Ocean, at the Bay of Bengal, values up to 4-5 mm/day higher than PI are observed. The results indicate a decrease in precipitation across the MMCT over the east African coast, between 0-20°N (0.5-2 mm/day lower), as well as drying at high latitudes (0-1 mm/day). Regarding SSTs, the highest values correspond to the MMCO experiment, with a mean global SST of 19.62°C, followed by the MMG experiment (18.04°C) and the PI experiment (16.85°C). The decrease in SST across the MMCT is

475 particularly evident in the southern high latitudes and the northern North Pacific (values up to 6-7°C lower).

8 Concluding remarks

The current study describes and provides a complete compilation of boundary conditions for GCMs characterizing the MMCO and the MMG periods. These boundary conditions include global topography, bathymetry and vegetation, and have a particular focus on the Antarctic ice-sheet and the South East Asian gateway. Besides, atmospheric CO_2 concentrations and
480 sea-level estimates were reviewed in detail. Other GCM input data, which strongly depend on the technical details of individual GCMs, like river routing, were not treated here, but can be constructed from the provided topographic datasets.

All data gathered in this study are available in the supplement, ready for use in GCMs. The compilation of boundary conditions for GCMs is time-consuming, especially when referring to deep time periods such as the Miocene. This assemblage of data can be used by the paleomodeling community as a base for a wide variety of Middle Miocene studies,
485 particularly for those related to the MMCT. Output data from two global climate model experiments using these boundary conditions were briefly described here, in order to proof the suitability of the new sets of boundary conditions for modeling purposes.

Despite ongoing efforts, the Middle Miocene is still a period with scarce data availability and thus the Middle Miocene picture presented here is inevitably subject to large uncertainties. More data, improved methods and higher resolutions are
490 required in order to improve the current boundary conditions and hence obtain more detailed and reliable model results.

9 Data availability

All the MMCO and MMG boundary conditions described above can be found in the supplement and at PANGAEA. The MMCO and MMG global topography/bathymetry data are available from the 2°x2° lat/lon grid files mmco_topo_bathy_v1_0.nc and mmg_topo_bathy_v1_0.nc, respectively. The MMCO and MMG global vegetation data can
495 be found in the 2°x2° lat/lon grid files mmco_veg_v1_0.nc and mmg_veg_v1_0.nc, respectively.

Acknowledgements

This research is part of the Marie Curie Initial Training Network Throughflow, funded by the E.U. 7th Framework Programme on Research, Technological Development and Demonstration. The CCSM3 simulations were performed on the Cray XC40/XC30 supercomputer of the Norddeutscher Verbund für Hoch- und Höchstleistungsrechnen (HLRN). We are
500 particularly grateful to Robert Hall, Nicholas Herold, David Pollard and Matthew Pound for their contributions in the assemblage of boundary conditions. We also want to acknowledge Lydie Dupont, Sandra Passchier and Matthew Huber for that. We are grateful to Gary Strand, Sam Levis, Esther Brady, Stephen Yeager, and in particular to Nan Rosenbloom (NCAR) for their help in the model setup procedure. A very special thanks goes to Gabriel Gaus and Lars Nerger (HLRN)

for their support in the execution of the model runs. Thanks also to Andreas Manschke for the IT support, to Ute Merkel and
505   Gerlinde Jung for sharing their expertise in CCSM3, and to Hanno Keil for his introduction to ArcGIS. We are also grateful
to the Throughflow Network, and the Bremen International Graduate School for Marine Sciences GLOMAR.

References

Billups, K. and Schrag, D. P.: Paleotemperatures and ice volume of the past 27 Myr revisited with paired Mg/Ca and $^{18}O/^{16}O$
measurements on benthic foraminifera, Paleoceanography, 17(1), 3–1–3–11, doi:10.1029/2000PA000567, 2002.

510   Billups, K. and Schrag, D. P.: Application of benthic foraminiferal Mg/Ca ratios to questions of Cenozoic climate change,
Earth Planet. Sc. Lett., 209(1–2), 181–195, doi:10.1016/S0012-821X(03)00067-0, 2003.

Bonan, G. B.: A Land Surface Model (LSM Version 1.0) for Ecological, Hydrological, and Atmospheric Studies: Technical
Description and User's Guide, NCAR Technical Note NCAR/TN–417+STR, National Center for Atmospheric
Research, Boulder, Colorado, 1–150, doi:10.5065/D6DF6P5X, 1996.

515   Collins, W. D., Bitz, C. M., Blackmon, M. L., Bonan, G. B., Bretherton, C.S., Carton, J. A., Chang, P., Doney, S. C., Hack,
J. J., Henderson, T. B., Kiehl, J. T., Large, W. G., McKenna, D. S., Santer, B. D. and Smith, R. D.: The Community
Climate System Model Version 3 (CCSM3), J. Clim., 19, 2122–2143, doi:10.1175/JCLI3761.1, 2006.

De Boer, B., Van De Wal, R. S. W., Bintanja, R., Lourens, L. J. and Tuenter, E.: Cenozoic global ice-volume and
temperature simulations with 1-D ice-sheet models forced by benthic $\delta^{18}O$ records, Ann. Glaciol., 51(55), 23–33,
520   doi:10.3189/172756410791392736, 2010.

DeConto, R. M., Pollard, D., Wilson, P. A., Paelike, H., Lear, C. H. and Pagani, M.: Thresholds for Cenozoic bipolar
glaciation, Nature, 455, 652–656, doi:10.1038/nature07337, 2008.

Duque-Caro, H.: Neogene stratigraphy, paleoceanography and paleobiogeography in northwest South America and the
evolution of the Panama seaway, Palaeogeogr. Palaeocl., 77(3–4), 203–234, doi:10.1016/0031-0182(90)90178-A,
525   1990.

Fairbanks, R. G. and Matthews R. K.: The marine oxygen isotope record in Pleistocene coral, Barbados, West Indies, Quat.
Res., 10(2), 181–196, doi:10.1016/0033-5894(78)90100-X, 1978.

Flower, B. P. and Kennett, J. P.: The middle Miocene climatic transition: East Antarctic ice sheet development, deep ocean
circulation and global carbon cycling, Palaeogeogr. Palaeocl., 108(3–4), 537–555, doi:10.1016/0031-
530   0182(94)90251-8, 1994.

Foster, G. L., Lear, C. H. and Rae, J. W. B.: The evolution of pCO_2, ice volume and climate during the middle Miocene,
Earth Planet. Sc. Lett., 341–344, 243–254, doi:10.1016/j.epsl.2012.06.007, 2012.

Gasson, E., DeConto, R. M., Pollard, D. and Levy, R. H.: Dynamic Antarctic ice sheet during the early to mid-Miocene, P. Natl. Acad. Sci., 113(13), 3459–3464, doi:10.1073/pnas.1516130113, 2016.

535   Ghosh, P., Garzione, C. N. and Eiler, J. M.: Rapid Uplift of the Altiplano Revealed Through $^{13}C–^{18}O$ Bonds in Paleosol Carbonates, Science, 311(5760), 511-515, doi: 10.1126/science.1119365, 2006.

Gordon, A. L., Giulivi, C. F. and Ilahude, A. G.: Deep topographic barriers within the Indonesian seas, Deep-Sea Res. II, 50(12–13), 2205–2228, doi:10.1016/S0967-0645(03)00053-5, 2003.

Greenop, R., Foster, G. L., Wilson, P. A. and Lear, C. H.: Middle Miocene climate instability associated with high-amplitude 540 CO_2 variability, Paleoceanography, 29(9), 845–853, doi:10.1002/2014PA002653, 2014.

Hall, R: Sundaland and Wallacea: geology, plate tectonics and palaeogeography, in: Biotic Evolution and Environmental Change in Southeast Asia, edited by Gower, D. J., Richardson, J. E., Rosen, B. R., Rueber, L. and Williams, S. T., Cambridge University Press, 32-78, 2012.

Hamon, N., Sepulchre, P., Lefebvre, V. and Ramstein, G.: The role of eastern tethys seaway closure in the middle miocene 545   climatic transition (ca. 14 Ma), Clim. Past, 9(6), 2687–2702, doi:10.5194/cp-9-2687-2013, 2013.

Haq, B. U., Hardenbol, J. and Vail, P. R.: Chronology of Fluctuating Sea Levels Since the Triassic, Science, 235(4793), 1156–1167, doi:10.1126/science.235.4793.1156, 1987.

Herold, N., Seton, M., Müller, R. D., You, Y. and Huber, M.: Middle Miocene tectonic boundary conditions for use in climate models, Geochem. Geophy. Geosy., 9(10), Q10009, doi:10.1029/2008GC002046, 2008.

550   Herold, N., Huber, M. and Müller, R. D.: Modeling the miocene climatic optimum. Part I: Land and atmosphere, J. Clim., 24, 6353–6372, doi:10.1175/2011JCLI4035.1, 2011.

Herold, N., Huber, M., Müller, R. D., Seton, M.: Modeling the Miocene climatic optimum: Ocean circulation, Paleoceanography, 27(1), PA1209, doi:10.1029/2010PA002041, 2012.

Holbourn, A., Kuhnt, W., Schulz, M. and Erlenkeuser, H.: Impacts of orbital forcing and atmospheric carbon dioxide on 555   Miocene ice-sheet expansion, Nature, 438(7067), 483–487, doi:10.1038/nature04123, 2005.

Holbourn, A., Kuhnt, W., Schulz, M., Flores, J. A. and Andersen, N.: Orbitally-paced climate evolution during the middle Miocene "Monterey" carbon-isotope excursion, Earth Planet. Sc. Lett., 261(3–4), 534–550, doi:10.1016/j.epsl.2007.07.026, 2007.

John, C. M., Karner, G. D., Browning, E., Leckie, R. M., Mateo, Z., Carson, B. and Lowery, C.: Timing and magnitude of 560   Miocene eustasy derived from the mixed siliciclastic-carbonate stratigraphic record of the northeastern Australian margin, Earth Planet. Sc. Lett., 304(3–4), 455–467, doi:10.1016/j.epsl.2011.02.013, 2011.

Kaplan, J. O.: Geophysical Applications of Vegetation Modeling, Ph. D. thesis, Lund University, Lund, 128 pp., 2001.

Kominz, M. A., Browning, J. V., Miller, K. G., Sugarman, P. J., Mizintseva, S. and Scotese, C. R.: Late Cretaceous to Miocene sea-level estimates from the New Jersey and Delaware coastal plain coreholes: An error analysis, Basin Research, 20(2), 211–226, doi:10.1111/j.1365-2117.2008.00354.x, 2008.

Krapp, M. and Jungclaus, J. H.: The Middle Miocene climate as modelled in an atmosphere–ocean–biosphere model, Clim. Past, 7(4), 1169–1188, doi:10.5194/cp-7-1169-2011, 2011.

Kuerschner, W. M., Kvacek, Z. and Dilcher, D. L.: The impact of Miocene atmospheric carbon dioxide fluctuations on climate and the evolution of terrestrial ecosystems, P. Natl. Acad. Sci., 105(2), 449–453, doi:10.1073/pnas.0708588105, 2008.

Kuhnt, W., Holbourn, A., Hall, R., Zuvela, M. and Kaese, R.: Neogene history of the Indonesian Throughflow, in: Continent-Ocean Interactions Within East Asia Marginal Seas, edited by Clift, P., Kuhnt, W., Wang, P., Hayes, D., Geophysical Monograph Series, 149, 299–320, doi:10.1029/149GM16, 2004.

Langebroek, P. M., Paul, A. and Schulz, M.: Antarctic ice-sheet response to atmospheric CO_2 and insolation in the Middle Miocene, Clim. Past, 5(4), 633–646, doi:10.5194/cp-5-633-2009, 2009.

Langebroek, P. M., Paul, A. and Schulz, M.: Simulating the sea level imprint on marine oxygen isotope records during the middle Miocene using an ice sheet-climate model, Paleoceanography, 25(4), PA4203, doi:10.1029/2008PA001704, 2010.

Laskar, J., Robutel, P., Joutel, F., Gastineau, M., Correia, A. C. M., Levrard, B.: A long term numerical solution for the insolation quantities of the Earth, 428, 261-285, A&A, doi:10.1051/0004-6361:20041335, 2004.

Lear, C. H., Elderfield, H. and Wilson, P.A.: Cenozoic Deep-Sea Temperatures and Global Ice Volumes from Mg/Ca in Benthic Foraminiferal Calcite, Science, 287(5451), 269–272, doi:10.1126/science.287.5451.269, 2000.

Lear, C. H., Mawbey, E. M. and Rosenthal, Y.: Cenozoic benthic foraminiferal Mg/Ca and Li/Ca records: Toward unlocking temperatures and saturation states, Paleoceanography, 25(4), PA4125, doi:10.1029/2009PA001880, 2010.

Levy, R., Harwood, D., Florindo, F., Sangiorgi, F., Tripati, R., von Eynatten, H., Gasson, E., Kuhn, G., Tripati, A., DeConto, R., Fielding, C., Field, B., Golledge, N., McKay, R., Naish, T., Olney, M., Pollard, D., Schouten, S., Talarico, F., Warny, S., Willmott, V., Acton, G., Panter, K., Paulsen, T., Taviani, M. and SMS Science Team: Antarctic ice sheet sensitivity to atmospheric CO_2 variations in the early to mid-Miocene, P. Natl. Acad. Sci., 113(13), 3453–3458, doi:10.1073/pnas.1516030113, 2016.

Lewis, A. R., Marchant, D. R., Ashworth, A. C., Hemming, S. R. and Machlus, M. L.: Major middle Miocene global climate change: Evidence from East Antarctica and the Transantarctic Mountains, Geol. Soc. Am. Bull., 119(11–12), 1449–1461, doi:10.1130/B26134.1, 2007.

Miller, K. G., Fairbanks, R. G. and Mountain, G. S.: Tertiary oxygen isotope synthesis, sea level history, and continental margin erosion, Paleoceanography, 2(1), 1-19, doi:10.1029/PA002i001p00001, 1987.

595   Montes, C., Cardona, A., McFadden, R., Moron, S. E., Silva, C. A., Restrepo-Moreno, S., Ramirez, D. A., Hoyos, N.,
          Wilson, J., Farris, D., Bayona, G. A., Jaramillo, C. A., Valencia, V., Bryan, J. and Flores, J. A.: Evidence for middle
          Eocene and younger land emergence in central Panama: Implications for Isthmus closure, Geol. Soc. Am. Bull.,
          124(5–6), 780–799, doi:10.1130/B30528.1, 2012.

       Morley, R. J.: Cretaceous and Tertiary climate change and the past distribution of megathermal rainforests, in: Tropical
600   Rainforest Responses to Climatic Change, Bush, M., Flenley, J., Gosling, W., Springer Praxis Books, Berlin,
          Heidelberg, 1-34, 2011.

       Oerlemans, J.: Correcting the Cenozoic δ^{18}O deep-sea temperature record for Antarctic ice volume, Palaeogeogr. Palaeocl.,
          208(3–4), 195–205, doi:10.1016/j.palaeo.2004.03.004, 2004.

       Otto-Bliesner, B. L., Tomas, R., Brady, E. C., Ammann, C., Kothavala, Z., and Clauzet, G.: Climate sensitivity of moderate
605   and low resolution versions of CCSM3 to preindustrial forcings, J. Climate, 19, 2567–2583,
          doi:10.1175/JCLI3754.1, 2006.

       Pagani, M., Zachos, J. C., Freeman, K. H., Tipple, B., Bohaty, S.: Marked Decline in Atmospheric Carbon Dioxide
          Concentrations During the Paleogene, Science, 309(5734), 600–603, doi:10.1126/science.1110063, 2005.

       Pearson, P. N. and Palmer, M. R.: Atmospheric carbon dioxide concentrations over the past 60 million years, Nature,
610   406(6797), 695–699, doi:10.1038/35021000, 2000.

       Pollard, D. and DeConto, R. M.: Description of a hybrid ice sheet-shelf model, and application to Antarctica, Geosci. Model
          Dev., 5, 1273-1295, doi:10.5194/gmd-5-1273-2012, 2012

       Pound, M. J., Haywood, A. M., Salzmann, U. and Riding, J. B.: Global vegetation dynamics and latitudinal temperature
          gradients during the Mid to Late Miocene (15.97–5.33Ma), Earth-Sci. Rev., 112(1–2), 1–22,
615   doi:10.1016/j.earscirev.2012.02.005, 2012.

       Ramstein, G., Fluteau, F., Besse, J. and Joussaume, S.: Effect of orogeny, plate motion and land-sea distribution on Eurasian
          climate change over the past 30 million years, Nature, 386, 788-795, doi:10.1038/386788a0, 1997.

       Retallack, G. J.: Refining a pedogenic-carbonate CO_2 paleobarometer to quantify a middle Miocene greenhouse spike,
          Palaeogeogr. Palaeocl., 281(1–2), 57–65, doi:10.1016/j.palaeo.2009.07.011, 2009.

620   Rögl, F.: Mediterranean and Parathethys. Facts and hypotheses of an Oligocene to Miocene paleogeography (short
          overview), Geologica carpathica, 50(4), 339–349, 1999.

       Rosenbloom, N., Shields, C., Brady, E., Levis, S. and Yeager, S.: Using CCSM3 for Paleoclimate Applications, NCAR
          Technical Note NCAR/TN–483+STR, National Center for Atmospheric Research, Boulder, Colorado, 1–81,
          doi:10.5065/D69S1P09, 2011.

625 Shevenell, A. E., Kennett, J. P. and Lea, D. W.: Middle Miocene ice sheet dynamics, deep-sea temperatures, and carbon cycling: A Southern Ocean perspective, Geochem. Geophy. Geosy., 9(2), Q02006, doi:10.1029/2007GC001736, 2008.

Thiede, J., Jessen, C., Knutz, P., Kuijpers, A., Mikkelsen, N., Nørgaard-Pedersen, N. and Spielhagen, R. F.: Millions of Years of Greenland Ice Sheet History Recorded in Ocean Sediments, Polarforschung, 80(3), 141–159, 2011.

630 Tong, J. A., You, Y., Müller, R. D. and Seton, M.: Climate model sensitivity to atmospheric CO_2 concentrations for the middle Miocene, Glob. Planet. Change, 67(3–4), 129–140, doi:10.1016/j.gloplacha.2009.02.001, 2009.

Tripati, A. K., Roberts, C. D. and Eagle, R. A.: Coupling of CO_2 and Ice Sheet Stability Over Major Climate Transitions of the Last 20 Million Years, Science, 326(5958), 1394–1397, doi:10.1126/science.1178296, 2009.

Wolfe, J. A.: Temperature parameters of humid to mesic forests of Eastern Asia and relation to forests of other regions of the
635 Northern Hemisphere and Australasia, U.S. Geological Survey professional paper, 1106, 1–37, 1979.

Wolfe, J.A.: Distribution of major vegetational types during the Tertiary, in: The carbon cycle and atmospheric CO_2: natural variations Archean to present, edited by: Sundquist E. T. and Broecker W. S., American Geophysical Union Monograph, 32, 357–375, doi:10.1029/GM032p0357, 1985.

You, Y., Huber, M., Müller, R. D., Poulsen, C. J. and Ribbe, J.: Simulation of the middle miocene climate optimum,
640 Geophys. Res. Lett., 36(4), L04702, doi:10.1029/2008GL036571, 2009.

Zachos, J., Pagani, M., Sloan, L., Thomas, E., Billups, K.: Trends, Rhythms, and Aberrations in Global Climate 65 Ma to Present, Science, 292(5517), 686–693, doi:10.1126/science.1059412, 2001.

Zachos, J. C., Dickens, G. R. and Zeebe, R. E.: An early Cenozoic perspective on greenhouse warming and carbon-cycle dynamics, Nature, 451(7176), 279–283, doi:10.1038/nature06588, 2008.

645 Zhang, Y. G., Pagani, M., Liu, Z., Bohaty, S. M. and DeConto, R.: A 40-million-year history of atmospheric CO_2, Philos. Trans. R. Soc. A, 371(2001), 20130096, doi:10.1098/rsta.2013.0096, 2013.

650

655

MMCO   **MMG**
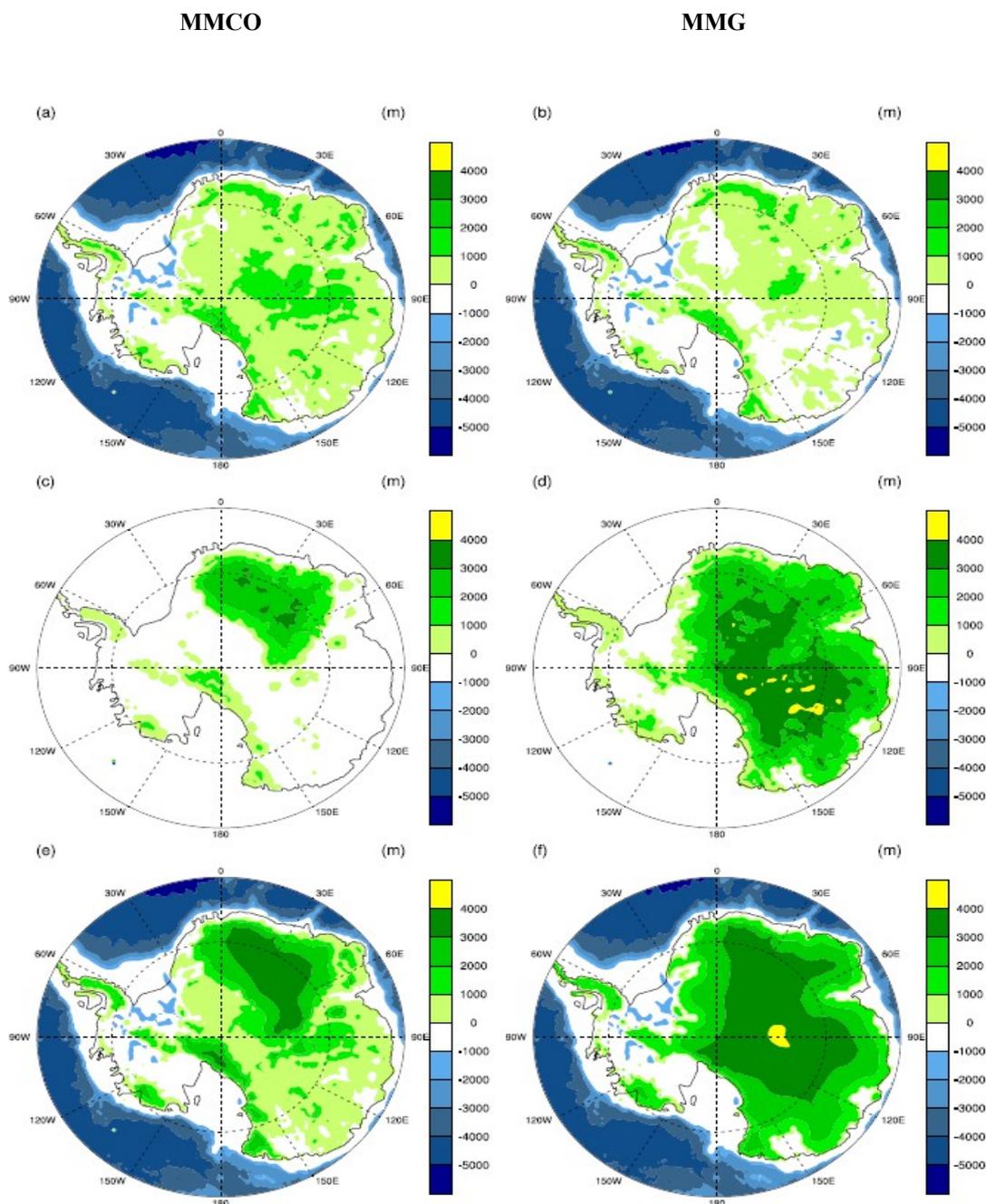
Figure 1: Reconstruction of Antarctica for the Middle Miocene Climatic Optimum (MMCO) and the Middle Miocene Glaciation
(MMG): (a), (b) bedrock elevation; (c), (d) ice thickness; (e), (f) total elevation (bedrock elevation + ice thickness), in meters. Black
lines represent present day coastline. Data from David Pollard.
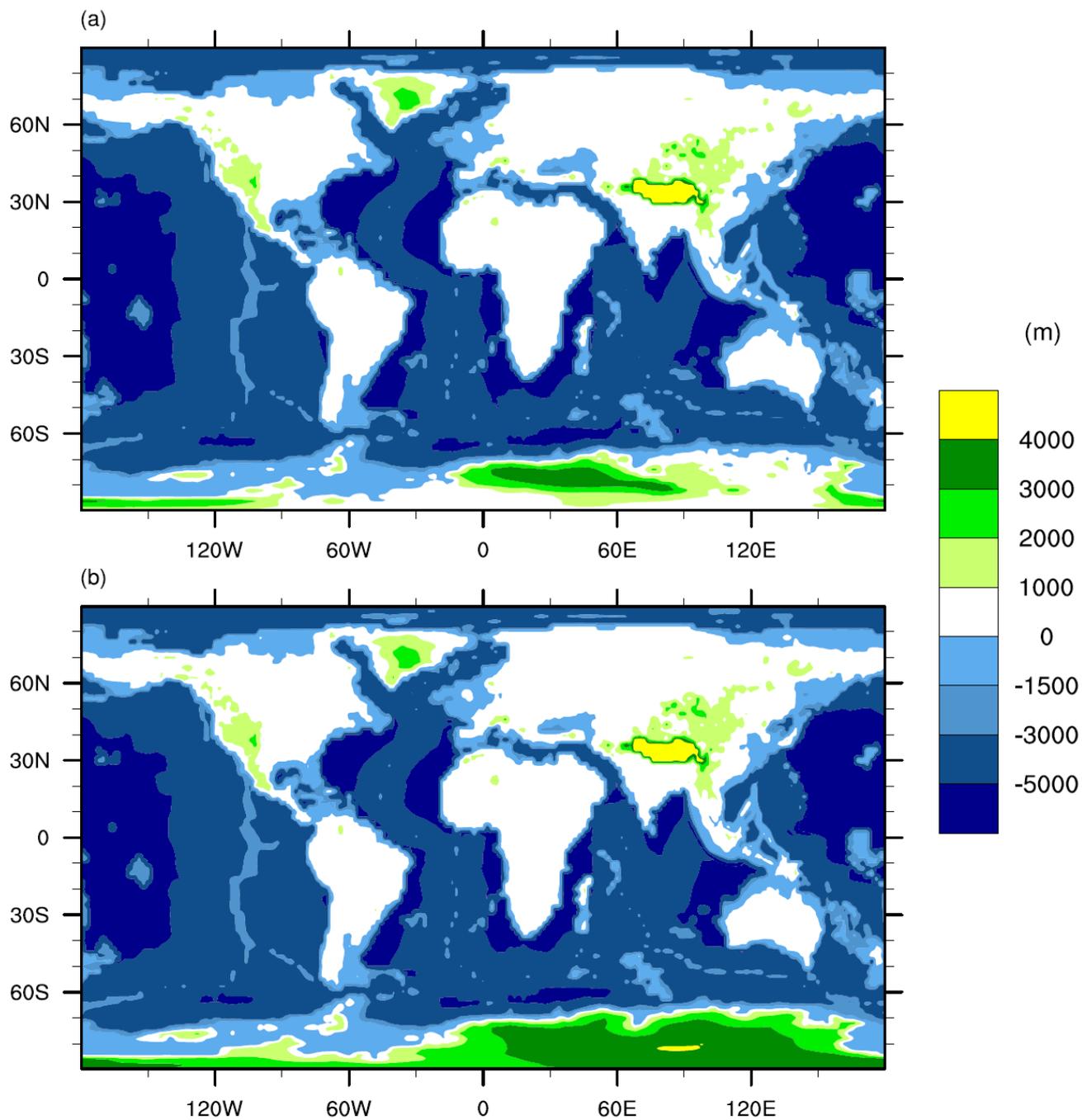
Figure 2: Topography/bathymetry reconstruction for the (a) MMCO and the (b) MMG.
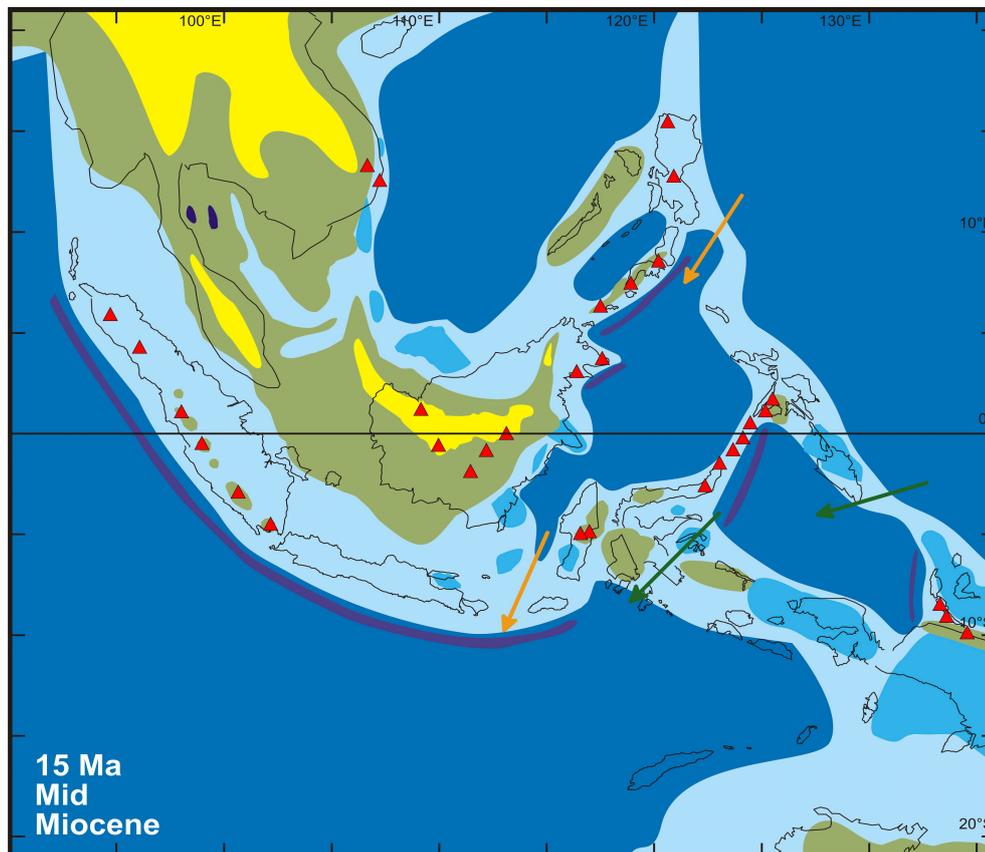
Figure 3: Paleogeographic reconstruction of South East Asia for 15 Ma from Hall (2012). Geographic features: volcanoes in red (triangles), highlands in yellow, land in green, carbonate platforms in blue, shallow sea in light blue, deep sea in dark blue,

665   **trenches in violet. Figure courtesy of Robert Hall (Royal Holloway, University of London). Arrows represent Middle Miocene postulated ocean paths across the Indonesian archipelago and are based on Kuhnt et al. (2004). Eastern paths shown in green, western paths in orange.**

670
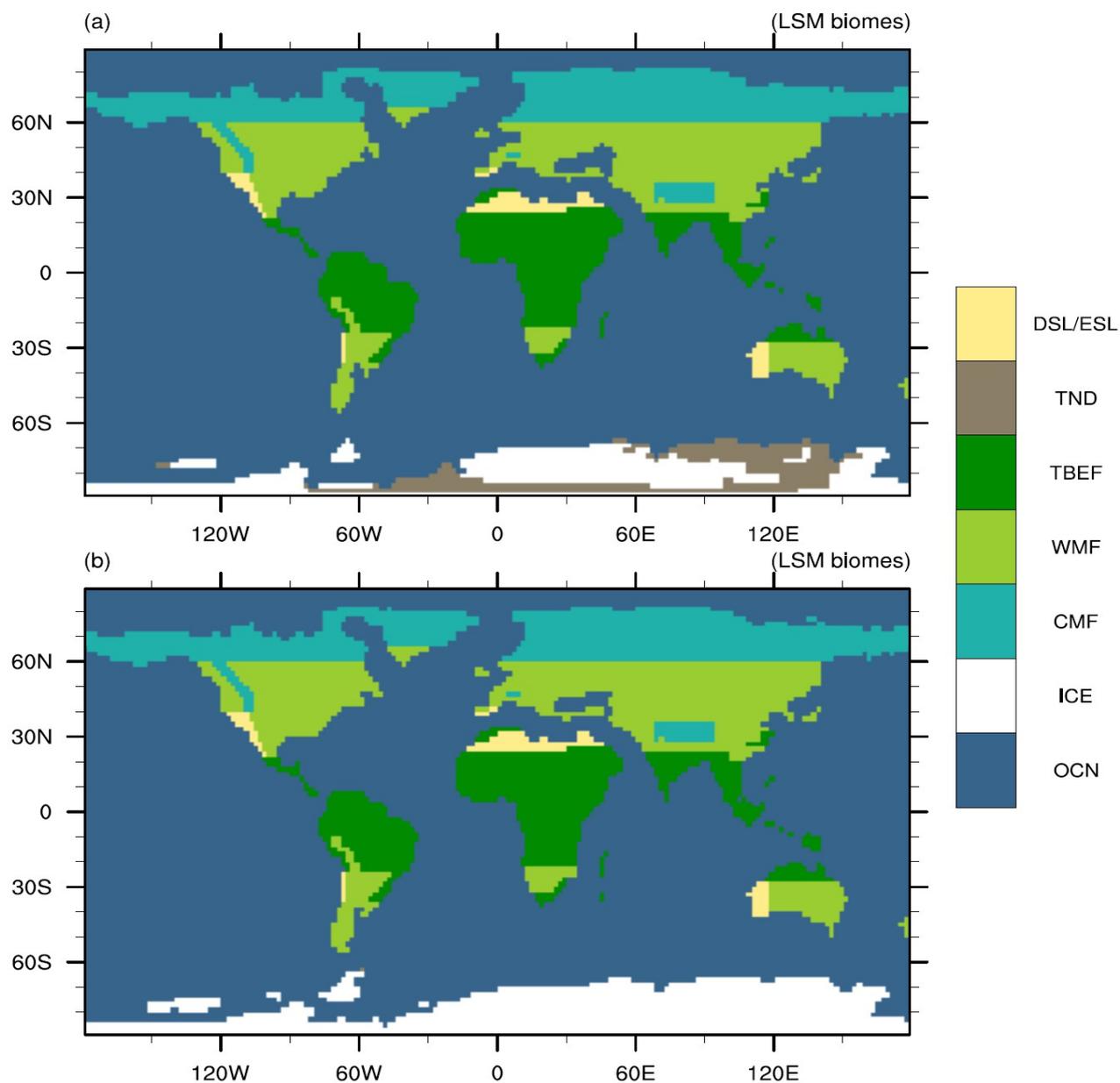
Figure 4: **Vegetation reconstruction for the (a) MMCO and the (b) MMG. Colors represent LSM biomes: CMF = cool mixed forest, WMF = warm mixed forest, TBEF = tropical broadleaf evergreen forest, TND = tundra, ESL = evergreen shrubland, DSL = deciduous shrubland, ICE = land ice, OCN = ocean.**
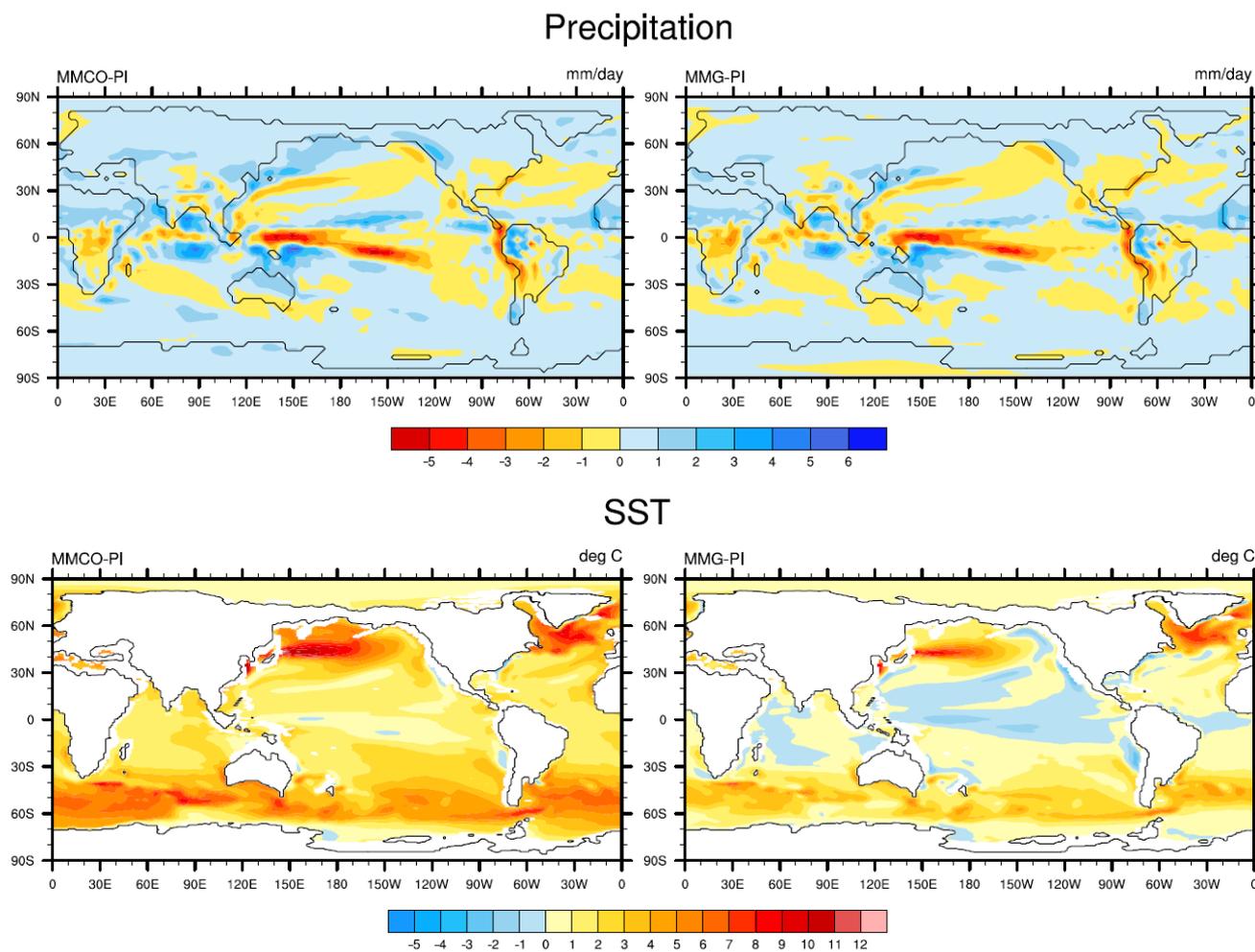
Figure 5: Sea-surface temperature (SST) (°C) and precipitation (in mm/day) differences between MMCO and MMG experiments, and PI, respectively.

	MMCO	MMG
Antarctic ice-sheet volume	6 million km³	23 million km³
Sea-level	48 m higher than at present-day	5 m higher than at present-day
Atmospheric CO_2 concentration	400 ppmv	200 ppmv
Global topography/bathymetry	mainly Herold et al. (2008) with modifications for tropical seaways (Hall, 2012; Montes et al., 2012) and the Antarctic ice-sheet	same as MMCO, but with global sea-level reduced by 43 m and an expanded Antarctic ice-sheet
Global vegetation	mainly Pound et al. (2012) with gaps filled according to Wolfe (1985) and Morley (2011); ice and tundra in Antarctica	same as MMCO, but with tundra removed in Antarctica

Table 1: **Summary of boundary conditions for the Middle Miocene Climatic Optimum (MMCO) and the Middle Miocene Glaciation (MMG).**

685

690

BIOME4	LSM
tropical evergreen broadleaf forest	tropical broadleaf evergreen forest
tropical deciduous broadleaf forest and woodland	tropical broadleaf deciduous forest
warm-temperate evergreen broadleaf and mixed forest	warm mixed forest[1]
cool-temperate mixed forest	cool mixed forest[2]
tropical savanna	savanna
temperate xerophytic shrubland	evergreen shrub land or deciduous shrub land
temperate deciduous broadleaf savanna	deciduous shrub land
temperate grassland	cool grassland
low- and high-shrub tundra	tundra
prostrate dwarf-shrub tundra	tundra
ice	land ice
Wolfe's (1979) classification	**LSM**
mixed coniferous forest	cool mixed forest[3]
tropical rain forest	tropical broadleaf evergreen forest
paratropical rain forest	tropical broadleaf evergreen forest[4]
Morley's (2011) classification	**LSM**
megathermal rain forest	tropical broadleaf evergreen forest
monsoonal megathermal forest	tropical broadleaf deciduous forest

Table 2: **Conversion of vegetation types to the LSM vegetation scheme.**

[1] The *warm-temperate evergreen broadleaf and mixed forest* may contain broadleaf evergreen trees, needleleaf evergreen trees and deciduous trees. The *warm mixed forest* contains needleleaf evergreen trees and deciduous trees, but not broadleaf evergreen trees. [2] The deciduous trees in the *cool-temperate mixed forest* are temperate, meanwhile the ones in the *cool mixed forest* are boreal. [3] The *mixed coniferous forest* is mainly needleleaf evergreen, but broadleaf trees are also present. These can be deciduous or evergreen. The *cool mixed forest* is formed by needleleaf evergreens and broadleaf deciduous. Broadleaf evergreens are not present. [4] The *paratropical rain forest* is mainly broadleaf evergreen, but it may contain some broadleaf deciduous and conifers.

695

700

705

710

Experiment	PI	MMCO	MMG
CO$_2$	280 ppmv	400 ppmv	200 ppmv
Other GHGs			
Aerosols		Otto-Bliesner et al. (2006)	
Solar constant			
Eccentricity		2.13×10^{-4}	2.13×10^{-4}
Obliquity	1950 A.D.	23.24°	23.24°
Precession		102.92°	102.92°

Table 3: Summary of greenhouse gases, aerosols, solar constant, and orbital configuration for the CCSM3 test experiments.